




Technical Note

Analysis of Seismic Impact on Hailuogou Glacier after the 2022 Luding Ms 6.8 Earthquake, China, Using SAR Offset Tracking Technology

Weile Li , Junyi Chen, Huiyan Lu, Congwei Yu *, Yunfeng Shan , Zhigang Li, Xiujun Dong and Qiang Xu 

State Key Laboratory of Geohazard Prevention and Geoenvironment Protection, Chengdu University of Technology, Chengdu 610059, China

* Correspondence: congwei_yu@cdut.edu.cn; Tel.: +86-187-0191-1323

Abstract: An Ms 6.8 earthquake struck Luding County, Ganzi Prefecture, Sichuan Province on 5 September 2022, with the epicenter about 10 km away from Hailuogou Glacier. How Hailuogou Glacier was affected by the earthquake was of major concern to society. Sentinel-1 SAR satellite imaging was used to monitor the glacier surface velocity during different periods before and after the Luding earthquake based on pixel offset tracking (POT) technology, which applies a feature-tracking algorithm to overcome the phase co-registration problems commonly encountered in large displacement monitoring. The results indicated that the velocity had a positive correlation with the average daily maximum temperature and the slope gradient on the small-slope surfaces. The correlation was not apparent on the steeper surfaces, which corresponded spatially with the identified ice avalanche region in the Planet images. It was deduced that this may be because of the occurrence of ice avalanches on surfaces steeper than 25°, or that the narrower front channel impeded the glacier's movement. The Luding earthquake did not cause a significant increase in the velocity of Hailuogou Glacier within a large range, but it disturbed the front area of the ice cascade, where the maximum velocity reached 2.5 m/d. Although the possibility of directly-induced destruction by ice avalanches after the earthquake was low, and the buffering in the downstream glacier tongue further reduced the risk of ice avalanches, the risk of some secondary hazards such as debris flow increased. The proposed method in this study might be the most efficient in monitoring and evaluating the effects of strong earthquakes on glaciers because it would not be limited by undesirable weather or traffic blockage.

Keywords: Luding earthquake; Hailuogou Glacier; remote sensing monitoring; pixel offset tracking; glacier movement



Citation: Li, W.; Chen, J.; Lu, H.; Yu, C.; Shan, Y.; Li, Z.; Dong, X.; Xu, Q. Analysis of Seismic Impact on Hailuogou Glacier after the 2022 Luding Ms 6.8 Earthquake, China, Using SAR Offset Tracking Technology. *Remote Sens.* **2023**, *15*, 1468. <https://doi.org/10.3390/rs15051468>

Academic Editor:
Salvatore Stramondo

Received: 21 November 2022
Revised: 26 February 2023
Accepted: 4 March 2023
Published: 6 March 2023



Copyright: © 2023 by the authors. Licensee MDPI, Basel, Switzerland. This article is an open access article distributed under the terms and conditions of the Creative Commons Attribution (CC BY) license (<https://creativecommons.org/licenses/by/4.0/>).

1. Introduction

An earthquake of Ms 6.8 struck Luding County, Ganzi Prefecture, Sichuan Province, on 5 September 2022. The epicenter was located within Hailuogou Glacier forest park in Moxi Town, Luding County (39.25°N, 102.08°E), at a depth of 16 km. The earthquake lasted for around 20 s, and its maximum intensity was IX degrees [1]. According to the Sichuan Earthquake Administration (2022), 6486 aftershocks were recorded as late as 14:00 BST, 22 October 2022, among which 18 were greater than Ms 3.0, and the largest one (Ms 5.0) occurred on 22 October in Luding [2]. Although the national earthquake emergency response ended on 13 September, the earthquakes and their secondary hazards caused 93 deaths, 25 missing people, and over 270 injuries in total [3]. Meanwhile, the large number of earthquake-triggering geological hazards, for example, landslides, destroyed many residential constructions and traffic facilities, blocking roads in some regions. Owing to the short distance between the epicenter and the Hailuogou Glacier (approximately 10km), the seismic effects on these glaciers triggered considerable concern both socially and academically. However, the traffic blockages prevented workers from assessing the glacier

damage on site. In addition, the constant cloudy weather limited the availability of clear optical satellite images. Thus, the emergency seismic impact assessment on Hailuoguo Glacier is required to be completed using remote sensing methods.

Many scholars focus on the study of large earthquakes and their coseismic geohazards using diverse methods regarding different aspects. The seismic hazard analysis of large earthquakes, taking those in Lake Van Basin in Turkey as an example, could be expressed by the probability exceedance of a given PGA value, which is a determination for risk priority assessment [4]. The Newmark displacement model is also commonly utilized in predicting the displacement of landslides [5–7], while a large earthquake may influence the glacier stability and increase the susceptibility of ice avalanches that can be estimated by waveform and response spectra [8]. To monitor earth deformation, which is important in seismic impact analysis, several remote sensing techniques have been implemented. For example, Wu et al., examined the deformation velocity of northern China over the past 20 years using GNSS [9], while Lazos et al., analyzed the crustal deformation before an earthquake sequence in central Greece using GPS data [10]. Moreover, the mechanisms of crustal deformation dynamics in the Tibetan Plateau have been a controversial topic for years, and the lithospheric rheological structures of this region could be inversed using GPS and InSAR data [11]. Lastly, synthetic aperture radar (SAR) is a commonly used method for surface deformation studies, including in the geohazard monitoring of, for instance, land surface displacement, glacier movement, and landslides, and its all-time and all-weather observation provides consistently available data [12–14]. Cai (2022) concluded that there are currently two common methods for surface deformation monitoring using SAR images [15]: pixel offset tracking (POT) and differential interferometric SAR (D-InSAR). D-InSAR is mainly utilized for measuring delicate deformation due to high accuracy, but spatial-temporal decorrelation and phase-decoupling errors restrict its usage in large deformation gradients [16,17]. The events with a large deformation gradient, such as glacier movement, are more suitable to be monitored by POT, which tolerates a greater deformation gradient. In this study, SAR data were selected instead of GNSS and GPS data because the previous studies comparing SAR with its counterparts' performance stated that SAR was superior because of its low cost, high sensitivity, and almost complete coverage [18,19]. Given that the glacier surface scatter may be modified after significant deformation, which may lead to altered phase information and make it hard to calculate the velocity using common radar interferometry [20], POT uses the phase correlation method (detailed in Section 2.3) and overcomes this problem to some extent. The advanced feature-tracking algorithm led to POT being the method used to analyze the glacier surface velocity in this study.

2. Materials and Methods

2.1. Study Area

2.1.1. Regional Geological Background

The study area is located in the Hengduan Range at the southeastern edge of the Tibetan Plateau. It is a typical alpine valley terrain with a wide altitude range (approximately 6570 m) from 980 m to 7556 m at Mount Gongga. The Dadu River runs through the study area from north to south with a significant river drop, contributing to abundant hydropower resources.

The outcrops in the Hailuoguo catchment area are mainly Permian and Triassic metamorphic rocks, metasedimentary and Yanshan–Himalayan-period magmatic rocks, and Quaternary Holocene moraine lacustrine accumulations. The metamorphic rocks include metamorphic sandstone, slate, tuff, and marble. The magmatic rocks mainly include black mica granite and plagioclase granite. The Quaternary Holocene moraine lacustrine deposits are dominated by gray to gray-brown clasts [21,22].

The study area is situated near the intersection of the Y-shaped fault zone consisting of the Xianshuihe Fault, Longmenshan Fault, and Anninghe Fault in western Sichuan (Figure 1). The triggering fault of this earthquake was identified as the Moxi Fault at the southeastern part of the Xianshuihe Fault, which is one of the most active faults

globally with a length of around 350 km [23]. The Xianshuihe Fault is a left-lateral slip fault, making up an essential part of the north–south active tectonic zone in China. A recent systematic report concluded that nine large earthquakes larger than M_s 7.0 have occurred along this fault since 1700 [24]. Given that the reoccurrence period of a large earthquake ($M_s > 7.0$) at the Moxi Fault was estimated to be approximately 300 years based on empirical observations [25], scholars predicted that the Moxi Fault had the potential for a large earthquake ($M_s > 7.0$) occurrence within 30 years [26].

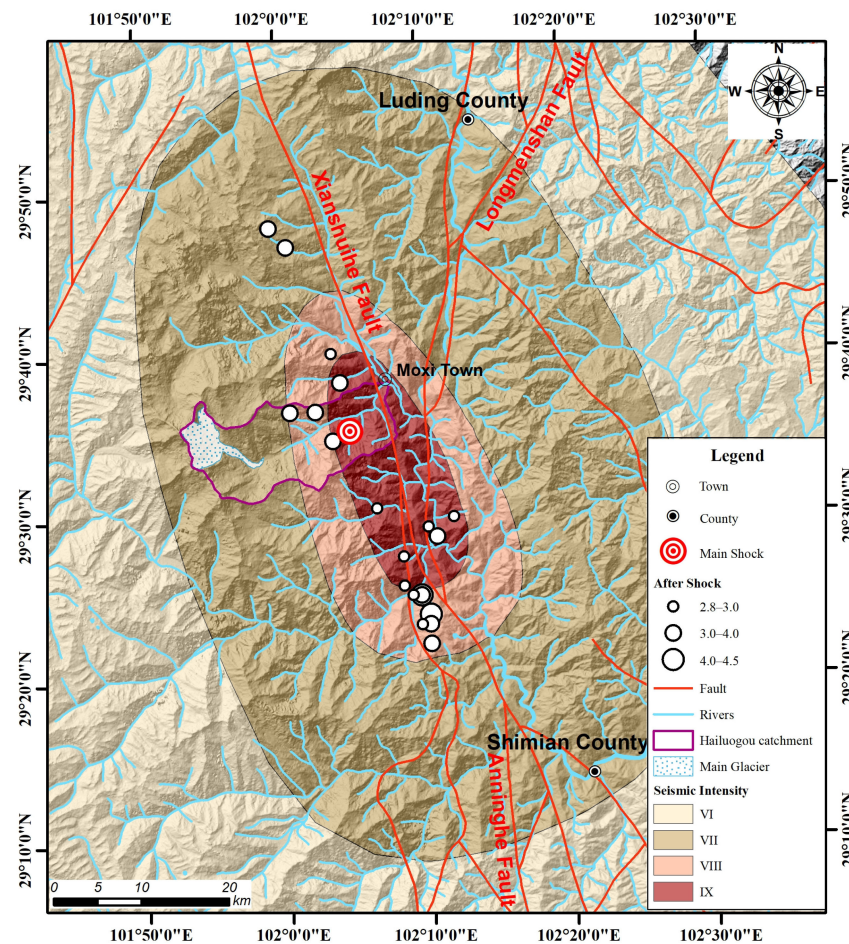


Figure 1. Geomorphologic and geological map of the Luding earthquake. The image of the fault is taken from the 1:500,000 geological map provided by the Sichuan Seismological Bureau, the seismic intensity information is taken from the Ministry of Emergency Management, and the seismic data are taken from the China Seismological Network Center.

2.1.2. Hailuogou Catchment Area

The Hailuogou catchment area is located on the eastern slope of Mount Gongga. It covers an area of approximately 195 km², and the altitude ranges from 1500 m to 7556 m (Figure 2). Figure 2 shows that the Luding earthquake triggered a considerable number of landslides, especially in the region near the epicenter. These landslides blocked the only access to the Hailuogou Glacier at several spots for a number of days. According to the drone aerial images shot on 14 September, which covered a 43 km² region from the gully mouth to the end of the glacier tongue, 656 coseismic geological hazards have been identified covering an area of 3.2 km², accounting for 7.4% of the total area (Figure 3).

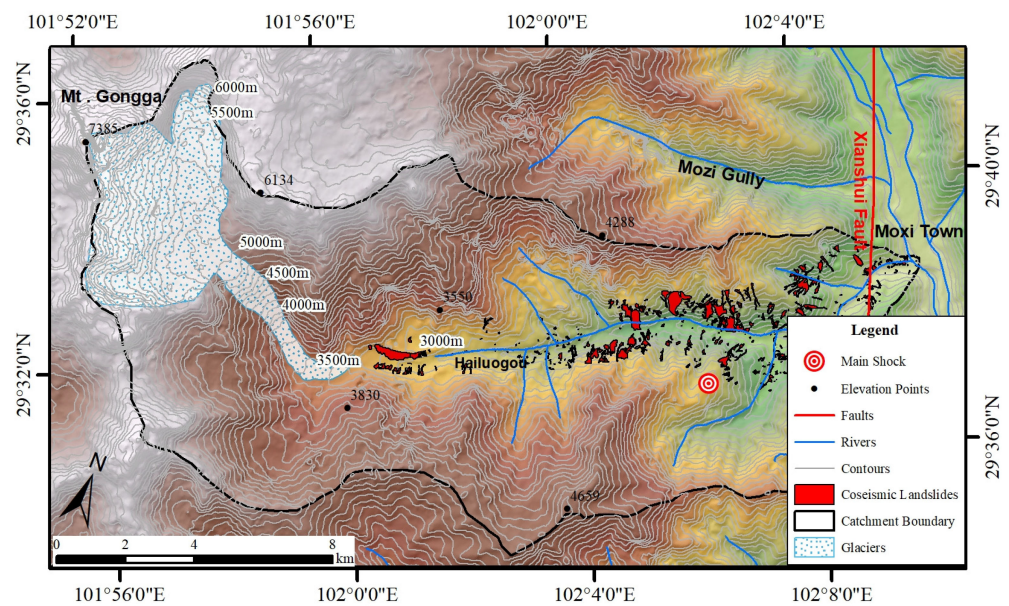


Figure 2. Geomorphologic map of Hailuoguo catchment area. The elevation ascends from the east (1500 m) to the west (7556 m). The Hailuoguo Glacier is located at the northwestern corner of the catchment area, while the east is mainly gullies.

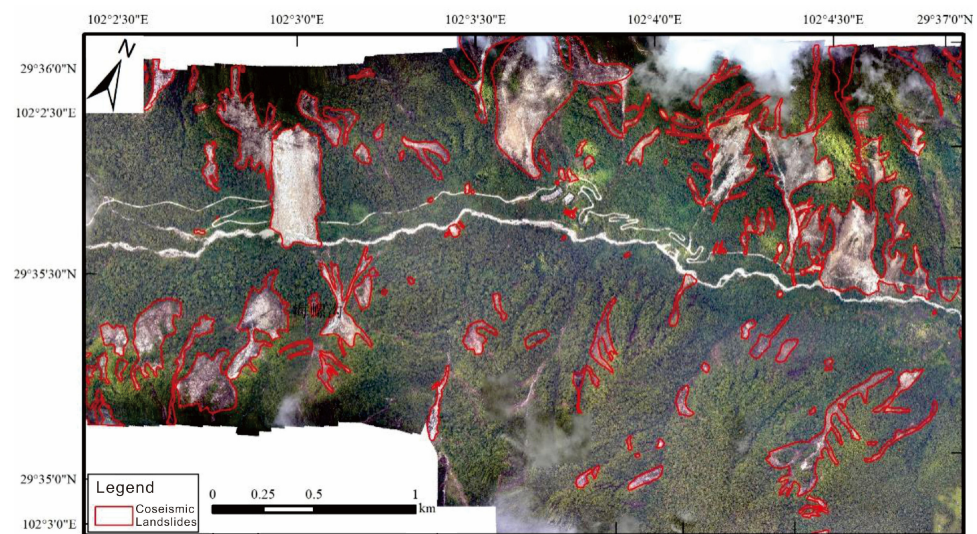


Figure 3. Distribution of coseismic landslides in the most severely struck region of Hailuoguo catchment area, shot by drone. A total of 656 identified coseismic geological hazards (3.2 km²) cover 7.4% of the whole range in this figure.

Hailuoguo Glacier is a typical monsoonal maritime temperate glacier with a length of 13.1 km and an area of 25.7 km² [27,28]. The glacier has retreated significantly under global climate changes. To be exact, the glacier has retreated 1822 m in the past 106 years, while the altitude of the end of the glacier in the Hailuoguo catchment area has risen by 300 m since 1823, with an annual average of over 1.6 m [29]. The Hailuoguo Glacier can be divided into three parts in sequence: firm basin (4980–7556 m a.s.l.), ice cascade (3700–4980 m a.s.l.), and glacier tongue (2900–3700 m a.s.l.), as shown in Figure 4a. The ice cascade used to be connected to the ice tongue; however, in recent years, they have been completely separated due to the constant thinning of the glaciers, forming a steep cliff with a vertical height difference of approximately 1080 m (Figure 4b). The landform of the firm basin is wide and gentle, where a great number of stacked glaciers from diverse directions continuously move downwards. When the moving glaciers reach the narrow gully upstream of the ice

cascade, where the slope increases rapidly, the glaciers converge and the front may become suspended, causing glaciers to be pulled and crevasses to develop, and thus, frequent ice avalanches form [30]. By comparing the multi-temporal Planet satellite images shown in Figure 5 [31], the moving crevasse indicates that at least four large-scale ice avalanches occurred in the ice cascade on 3 April 2018, 18 August 2018, 30 April 2022, and 29 July 2022, respectively.

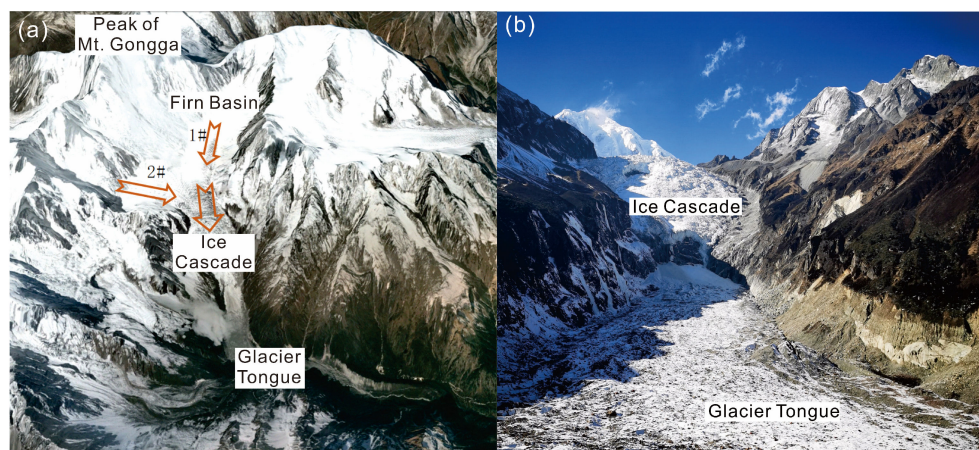


Figure 4. Satellite image and photo of the Hailuoguo Glacier. (a) Three-dimensional image of Hailuoguo Glacier (shot on 23 December 2017), where the arrows with tag 1# and 2# represent the two main directions of surface movement in the firn basin, and the other arrow stand for the movement direction on ice cascade; (b) photo of Hailuoguo Glacier (shot on 3 February 2021).

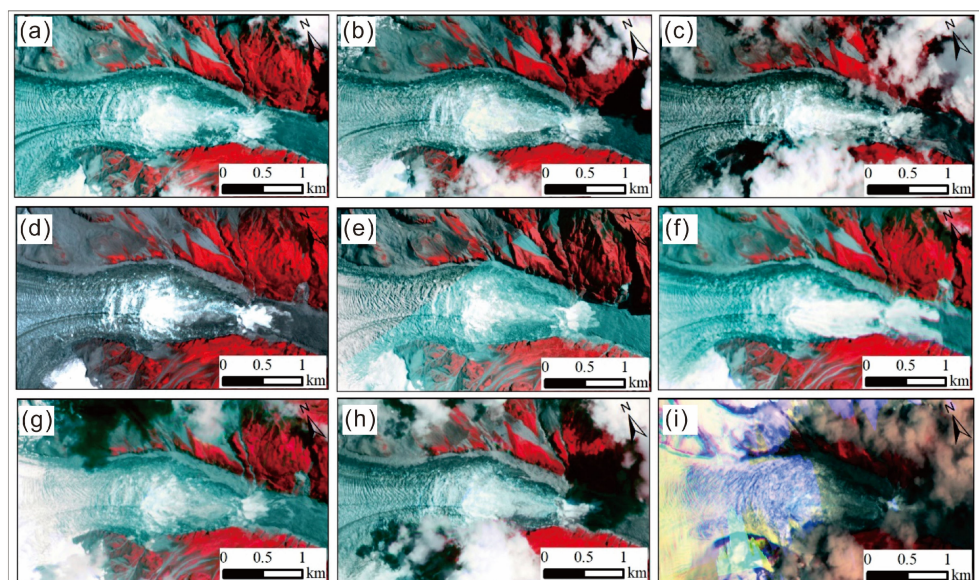


Figure 5. Changes of the ice cascade in the multi-temporal Planet satellite images. The shooting dates were (a) 17 August 2016, (b) 8 August 2017, (c) 31 August 2018, (d) 16 August 2019, (e) 26 August 2020, (f) 3 August 2021, (g) 29 July 2022, (h) 21 August 2022, and (i) 12 September 2022. The false color images (near-infrared, red, and green bands combination) distinguish the glaciers (in blue-green color) and vegetation (in red color), and they emphasize the occurrence of ice avalanche (in white color).

2.2. Data

A total of fourteen Sentinel-1 Radar images provided by the European Space Agency (ESA) were downloaded [32], among which eight were taken in 2020 or 2021 to monitor the

deformation characteristics of Hailuoguo Glacier under non-seismic effects by comparison, and the remaining six were taken before and after the earthquake in 2022 to assess the extent to which the Hailuoguo Glacier was affected by the earthquake. As Table 1 shows, a total of eleven periods of deformation were observed from the temporally adjacent SAR images. Using a C-band synthetic aperture radar, the Sentinel-1 radar satellite provides all-time and all-weather images [33]. The SAR data processed using the interferometric wide-swath (IWS) mode with a spatial resolution of $5\text{ m} \times 20\text{ m}$ were selected as the experimental data for the study of the glacier's movement.

Table 1. Eleven deformation-monitoring periods and their corresponding dates.

Year	Period Number	Date
2020	I	12 August 2020–24 August 2020
2021	II	14 July 2021–26 July 2021
	III	26 July 2021–7 August 2021
	IV	7 August 2021–19 August 2021
	V	19 August 2021–31 August 2021
	VI	31 August 2021–12 September 2021
2022	VII	9 July 2022–21 July 2022
	VIII	21 July 2022–2 August 2022
	IX	2 August 2022–14 August 2022
	X	14 August 2022–26 August 2022
	XI	26 August 2022–7 September 2022

Based on the Sentinel-1 data of ascending tracks, the layover and the shadow areas are plotted in Figure 6, which demonstrates that the identified glacier area was 24.98 km^2 , while the layover and shadow areas were 1.00 and 3.22 km^2 , accounting for 4% and 12.89% of the total study area, respectively.

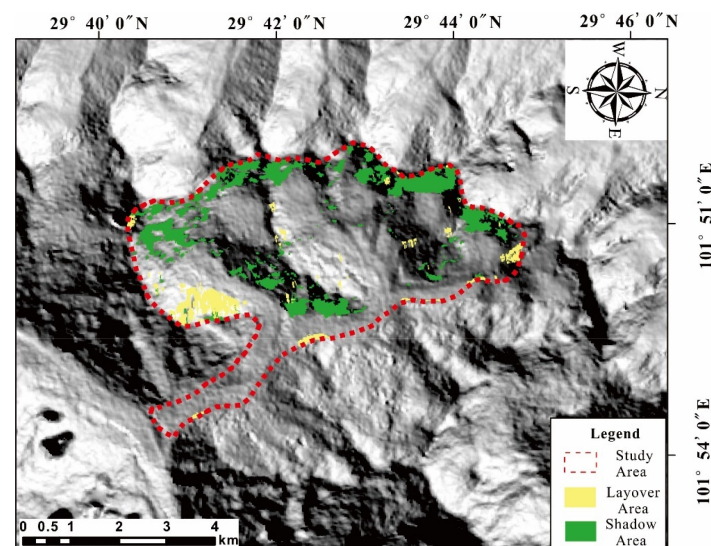


Figure 6. Shadow and layover area of SAR data in this study.

In addition to the SAR data, the temperature data were also essential in determining the relationship between the glacier movement and the temperature. In this study, the recorded temperature data of Luding County were regarded as the experimental data. They were downloaded from a public weather website called Tianqi [34], which provides historical meteorological data for cities in China.

2.3. Deformation Monitoring Method: POT

As mentioned in the previous section, POT is suitable for large deformation gradient monitoring, such as glacier movement. POT works based on tracking the offset of corresponding pixels in respect of either the intensity or coherence of two co-registered SAR images [20,35]. In this study, the SAR data from Sentinel-1 were chosen to investigate the glacier moving velocity by applying the intensity tracking procedure. The offset in the intensity tracking procedure is generated by estimating the normalized crossing correlation of the image patches in the SAR intensity images, which aims to determine the peak of the correlation function to identify the offset between the searching window and the target window [36]. To increase the estimation accuracy, oversampling rates were used in patch sampling and a 2D regression was determined by a four-point interpolation to simulate the correlation function around the peak [37]. The extent to which the local image offsetting is successfully estimated is determined by whether almost-identical characteristics exist within the chosen patch size in the two SAR images [36]. The reliability of the offset estimation can be assessed by the signal-to-noise ratio, calculated by comparing the peak height and the average of the correlation function [36].

Estimating glaciers’ deformation should consider the impacts from both the slant-range direction and the azimuth direction, which are related to the satellite orbiting configurations and the displacement caused by the two acquired SAR images’ temporal difference [36]. In cases of limited topography relief and length of baseline, the overall offset derived from the intensity tracking consists of the glacial offset and the orbital offset [37]. Therefore, the orbital offset is supposed to be excluded to obtain the glacial offset. In this study, bilinear polynomial functions were used to model the orbital offset:

$$\text{off}_R = a_0 + a_1x + a_2y + a_3xy \tag{1}$$

$$\text{off}_A = b_0 + b_1x + b_2y + b_3xy \tag{2}$$

where off_R and off_A represent the orbital offset in the slant-range direction and the azimuth direction, respectively; x and y represent the column and row number of the pixel in the plural images in a single vision; and a_i and b_i are the coefficients in the slant-range direction and the azimuth direction to be determined by the least square principle [37].

In this study, multi-temporal optical and Sentinel-1 SAR data obtained before and after the earthquake in the glacial region of the Hailuogou catchment area were collected from the Planet platform [31] and ESA [32], respectively. Subsequently, the glacier moving velocity changes were generated using POT. The general procedures are plotted in Figure 7. This paper focuses on the risk evaluation of potential post-seismic geological hazards, for example, ice avalanches and debris flow, based on the glacier velocity alternations after the Luding earthquake.

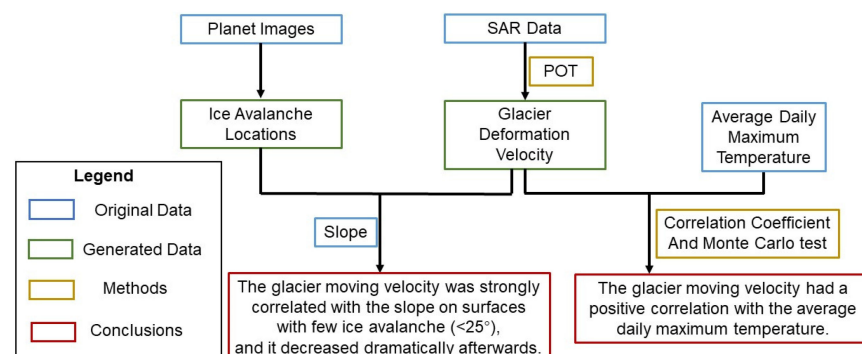


Figure 7. General flowchart of this study.

3. Results

The POT results of period XI are displayed in Figure 8. This graph indicates that the earthquake caused glaciers located on the eastern side of the peak of Mount Gongga, including gullies called Hailuogou, Mozigou, Yanzigou, Nanmengou, and their rear mountains, to become dramatically deformed, while those on the western side were relatively less affected. The ice cascade in the Hailuogou catchment area deformed the most, with a significant deformation area of about 1.5 km². The largest deformation in this area reached 30 m, and the maximum average moving velocity was approximately 2.5 m/d. The following sections focus on the POT result comparison and analysis of this significant deformation zone.

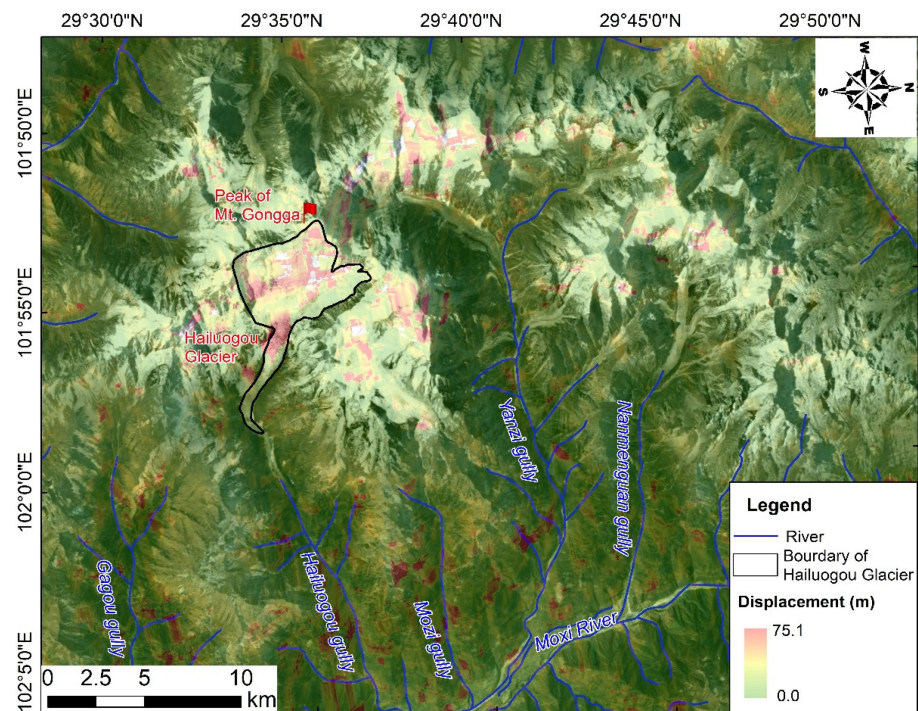


Figure 8. POT deformation result of Sentinel-1 SAR images between 26 August and 7 September 2022.

Firstly, the significant deformation zone was defined according to the deformation rendering map of each period with a displacement threshold of 6.0 m (Figure 9). The significant deformation area had an overall upward trend over the periods, and its maximum deformation value also increased. Subsequently, Figure 10 compares the areas of significant deformation in the corresponding periods in 2021 and 2022, showing that the areas were similar from July to August in both years at the level of about 0.6 km², while those in 2022 were slightly higher than their counterparts in 2021. The difference became obvious from late August to early September, during which the earthquake was the control variable. The assumed reason for the increment in August 2022 would be the higher average maximum temperature of August 2022 (30.55 °C) compared with that of the corresponding period in 2021 (26.84 °C), which is a difference of 3.71 °C. Furthermore, the constantly rising temperature in 2022 could also promote the movement of glaciers, leading to the significant expansion of the deformation area. Without the impact of the earthquake, the significant deformation area decreased in September 2021. By contrast, the significant deformation area continued to increase in the same period of 2022. Therefore, it can be deduced that the significant deformation area was strongly affected by the seismic shaking.

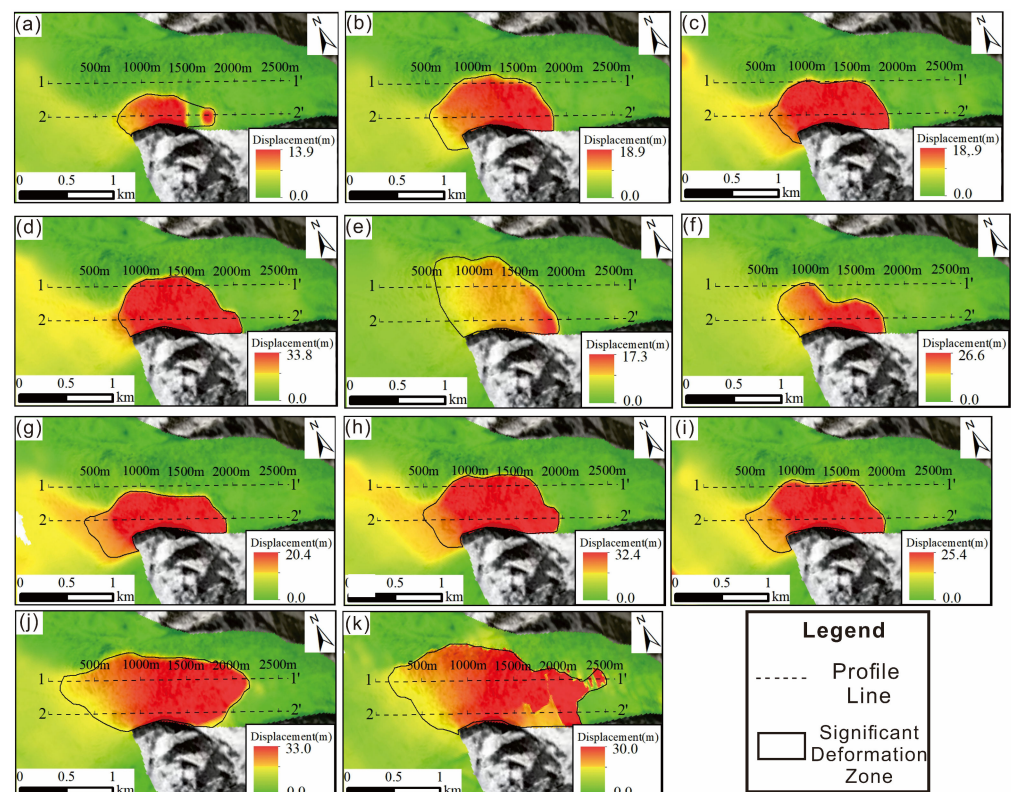


Figure 9. POT deformation results of Sentinel-1 SAR images of different periods. The base map is a Planet satellite image taken on 29 July 2022, and subgraphs (a–k) represent periods I–XI, respectively.

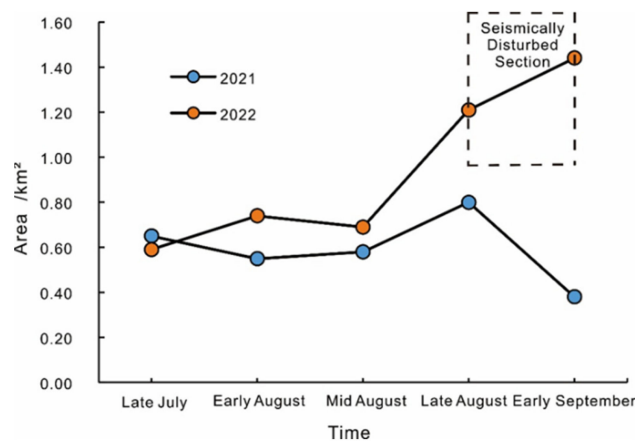


Figure 10. Area change of the significant deformation zone.

To further understand the deformation characteristics in the significant deformation zone, profile lines 1-1' and 2-2' at the central axis of the significant deformation zone in the XI and VIII periods, respectively, were added as the reference locations of the average velocity curve in Figure 11. On profile line 1-1', periods I to IX shared a similar trend of deformation along this line: there was slight movement at 0–700 m and the velocity increased steeply at 700–1100 m, reaching the top at around 1550 m after a slight drop. The velocities descended dramatically after this until maintaining less than 0.12 m/d at 1880 m. In contrast, the trends of the velocities in the 1–1300 m section were almost the same during the X and XI periods, which both increased from 0.5 m/d to 1.0 m/d. Following this, the velocity of the X period rose rapidly until 1880 m at a speed of 2.7 m/d before dropping dramatically, reaching 0.1 m/d at 2200 m. The velocity during the XI period increased rapidly from 1500 m at 1.2 m/d to 1810 m at 2.3 m/d, after which it fluctuated downwards.

Turning to the profile line 2-2', the velocities of all periods increased at a similar rate at 0–1300 m. Most of the velocities in periods I–X continued to increase over the following 400 m at different rates, dropping dramatically from the top at around 1690 m to less than 0.11 m/d at 2100 m. Lastly, the velocity in period XI descended gradually after the common trend of 0–1300 m and fluctuated at around 1700 m. After 2000 m, the velocity increased until 2150 m when it started to drop drastically. To summarize, the velocities of period XI in both sections had a significantly higher value in the seismic disturbed section compared with the other time periods.

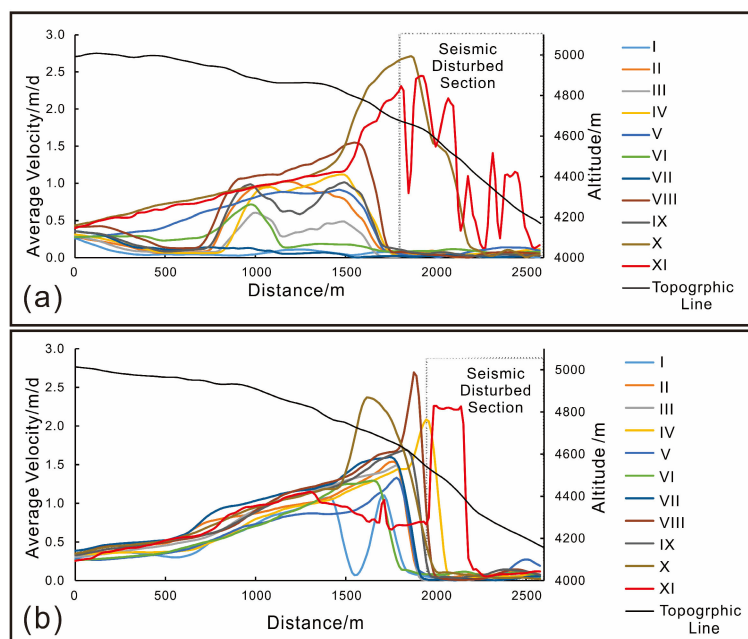


Figure 11. Average glacier moving velocities of the (a) 1-1' and (b) 2-2' profile lines.

4. Discussion

Before discussing the POT result, an error analysis should be made. Tazio Strozzi et al. (2022) concluded that the offset estimation errors are approximately $1/20$ of a pixel in both the slant-range and azimuth directions [37]. Given that the pixels in this study are $20\text{ m} \times 5\text{ m}$, the offset estimation error would be $\sqrt{\left(20 \times \frac{1}{20}\right)^2 + \left(5 \times \frac{1}{20}\right)^2} \approx 1.03\text{ m}$. Moreover, as shown in Figure 9, the estimated value reached 30 m, especially in 2022, which is the period focused upon in this study. Therefore, the error rate would be $1.03/30 \approx 3.4\%$ in the estimated offset, which could be extended to the estimated surface velocity.

The reliability of the POT result is another crucial issue worth discussing. Liu et al. (2019) utilized 38 PALSAR-1/2 images provided by the ALOS satellite during 2007–2018, applying POT to obtain the glacier's deformation velocity [27]. Liu et al. (2019) found that the velocity of the ice cascade and its upstream area was 1.2 m/d, and the fastest part moved at 2.5 m/d [27]. By contrast, the largest velocity measured in this study was 2.7 m/d in the profile line 1-1' before the earthquake, which was comparable with Liu et al.'s finding. Therefore, the estimated movement of the 11 glaciers calculated by Sentinel-1 data in this study should be generally reasonable.

The slope along the profile line 1-1' is plotted in Figure 12. Combined with the glacier moving velocity (Figure 11a), the significant deformation zone can be divided into two parts from top to bottom based on the correlation between velocity and slope: the correlated section (0–1880 m) and the slightly moving section (1880–2600 m), as shown in Figure 13. Specifically, the velocity was relatively less in the first 700 m where the slope was low. In the rest of the correlated section, the velocities of periods I–IX fluctuated with their slopes at the corresponding location on profile line 1-1', until the velocity dropped to the minimum

at 1880 m and was maintained in the remaining section. However, the velocities of periods X and XI obviously differed from the others in the slightly moving section, which dropped from an extreme maximum with fluctuation (XI).

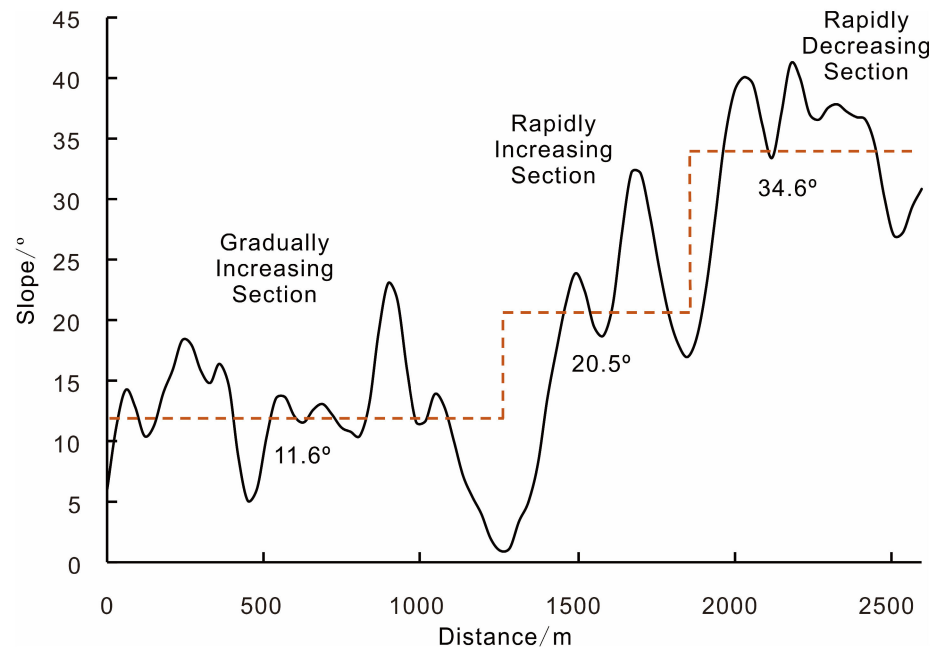


Figure 12. Mean slope and velocity trends on 1-1' profile line. The black curve stands for the slope values along the profile line 1-1', while the yellow dashed line depicts the average slope levels on different sections of the profile line.

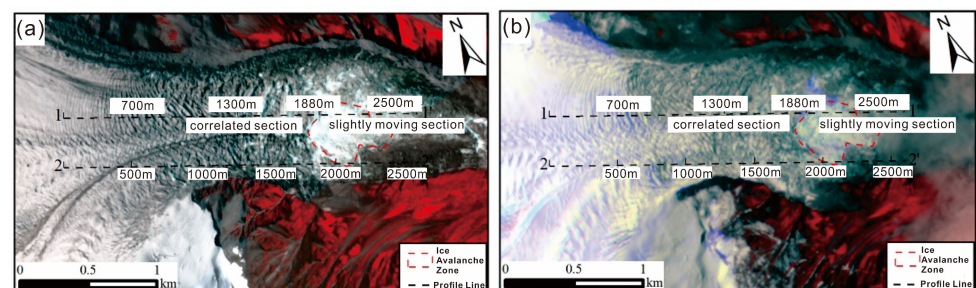


Figure 13. Planet satellite images of the ice cascade (a) before and (b) after the Luding earthquake.

The comparison between the Planet images with a resolution of 3.0 m before and after the earthquake revealed that the glacier surface within the correlated section had cracks, while the slightly moving section corresponded with the area prone to ice avalanches (Figure 13). Furthermore, Alean (1985a) stated that temperate glaciers can produce ice avalanches from an inclination of 25° or more [38]. The average slope in the slightly moving area (34.6°) was higher than the threshold, verifying the potential for ice avalanche occurrence. Therefore, it can be deduced that the glacier moving velocity was strongly related to the slope: the glacier moving velocity ascended with the slope increment until the velocity was maintained at a low level in the area prone to ice avalanches.

There are two reasons for the rapid decrement in the velocity on the ice cascade. Firstly, the potential ice avalanches on these steep slopes may result in missing corresponding pixels on the multi-temporal SAR images, thus lowering the signal-to-noise ratio of the POT offset estimation and distorting the results [27]. Secondly, Figure 14 indicates that the middle section of the ice cascade was wider than the upstream and downstream counterparts: the largest width in the middle section was 1100 m, while those of the upstream and downstream sections were only 850 and 580 m, respectively, which was only

half of that in the middle part. The width disparity along the ice cascade may impede the glacier's movement, leading to a rapid decrement in moving velocity at the narrow point. The constant accumulation of the glaciers from the trailing edge might contribute to the instability of the glaciers.

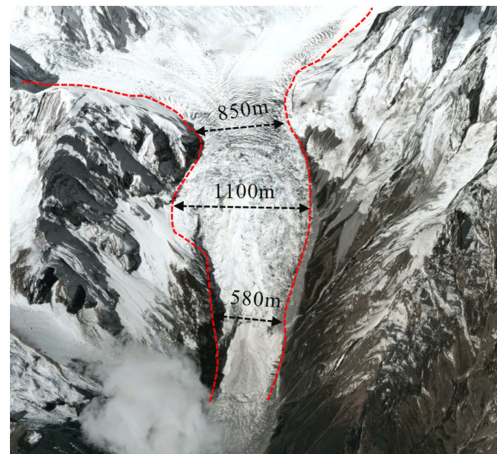


Figure 14. Three-dimensional remote sensing image of the ice cascade.

The 3 m resolution Planet optical satellite image comparison before and after the earthquake is shown in Figure 15. In these images, the difference between (a) and (b) provides evidence of the occurrence of ice avalanches. The visually abnormal region is related to the 1880–2500 m region in Figure 13, which is the seismic-disturbed area in Figure 11. Hence, it can be summarized that the seismic-disturbed area in Figure 11 was mainly distributed at the front of the ice cascade (1880–2500 m in Figure 13), where an ice avalanche occurring here (Figure 15) may be the cause of the change in velocity.

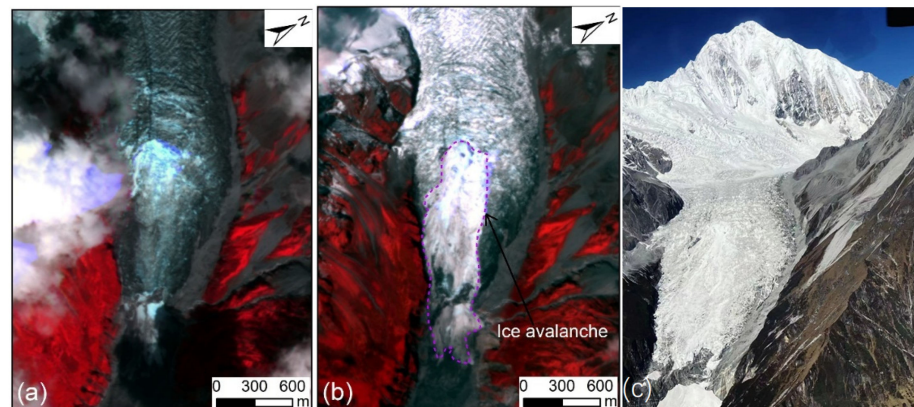


Figure 15. Ice avalanche identified using Planet optical satellite images taken on (a) 21 August 2022 and (b) 1 October 2022, and (c) an aerial photo taken on 20 October 2022.

In addition to the slope, the average daily maximum temperature also influenced the glacier's moving velocity. The average daily maximum temperatures of the latest four periods (VIII, IX, X, XI) in the significant deformation zone were calculated, which were 25.46 °C, 31.38 °C, 32.08 °C, and 24.5 °C, respectively. After calculating the correlation coefficients between the moving velocity of each pixel in the significant deformation zone during the four periods and their average daily maximum temperature, the Monte Carlo testing showed that the positive correlation between the velocity and temperature existed in about 83% of the significant deformation zone under a confidence level of $\alpha = 0.1$. The visualization of the correlation coefficient is displayed in Figure 16, which indicates that the positive correlation was mostly distributed in the velocity- and slope-correlated

area, while the velocity in the slightly moving area, which might be affected by the ice avalanches, appeared to be negatively correlated with the temperature. Therefore, it can be assumed that the glacier moving velocity is positively correlated with the temperature in the area with very few ice avalanches, and the correlation becomes unapparent on surfaces with larger slopes, indicating that the occurrence of ice avalanches might influence the derived surface velocity. In this study, the SAR offset tracking method provides evidence of quantitative analysis on the impact on glaciers after a large earthquake without the limitation of weather and traffic accessibility, which could be regarded as the most efficient method for the analysis of seismic impact on glaciers.

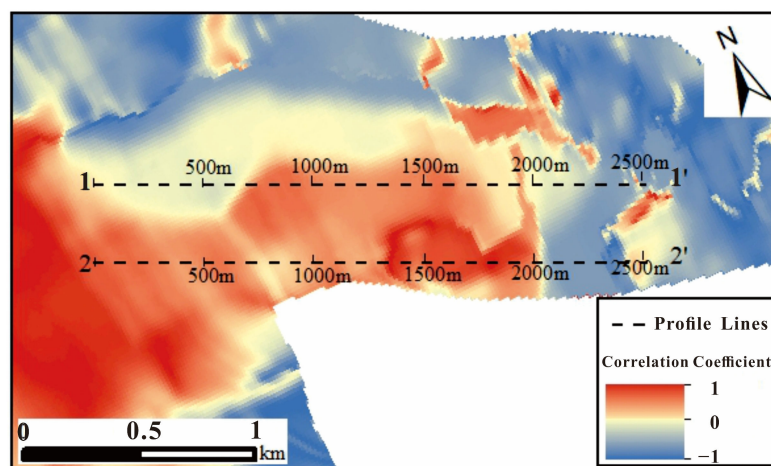


Figure 16. Correlation coefficients within the significant deformation zone.

Although ice avalanches may have occurred after the earthquake, the wide and relatively flatter glacier tongue downstream, as shown in Figure 4, is an ideal buffer for the substance from an ice avalanche, which reduced the risk of earthquake-triggered ice avalanches directly affecting the locals. However, substantial earthquake-induced landslides may contribute to debris flow. Specifically, the strong shaking of the earthquake downsized the sediment particles in the gully, leading to the rainfall threshold of the landslide being reduced dramatically [39]. In addition to the reduced rainfall threshold, the earthquake-triggered alternation in the infiltration, runoff, and confluence condition of the surface water promoted the flood peak [40], while the increasing sediment narrowed the gully's width [39]. Hence, the substantial sediment in the gully, the reduced gully width, and the lower rainfall threshold for debris flow provided ideal conditions for the formation of debris flow. The earthquake triggered landslides, which, theoretically, increased the sediment in the gully. Thus, if intensive rainfall occurs in this region, there will be a significant probability of debris flow. To reduce the risk of secondary hazards, the sediment in the gully should be cleared out before the storm period, which is an aspect worth considering. Moreover, taking the Guxiang debris flow as an example, the catastrophic debris flow occurred three years after the 1950 Ms 8.5 earthquake in Chayu, Tibet, China. The earthquake-triggered ice avalanches carried moraine and blocked the Yarlung Zangbo River, until the extreme rainfall and continuous high temperatures increased the runoff, putting considerable pressure on the dam, which then collapsed. The dam body and the saturated sediment were washed out, forming the debris flow with a volume of 106 m^3 , and the flow reached $28,600 \text{ m}^3/\text{s}$ [41]. Therefore, if large ice avalanches have occurred in Hailuoguo Glacier, emergency prevention is crucial to avoid hazardous cascades, such as the Guxiang debris flow, triggered by extreme weather in the future, such as conducting site investigations and clearing debris.

5. Conclusions

This study utilized Sentinel-1 satellite images to analyze the Hailuogou Glacier's moving velocity over diverse periods utilizing POT, and the findings are as follows:

(1) The significant deformation zone (about 1.5 km²) of the Hailuogou Glacier was mainly distributed within the ice cascade with a maximum average moving velocity of 2.5 m/d. The significant deformation zone can be divided into two parts from the top to bottom based on the correlation between velocity and slope: the correlated part and the slightly moving part. There are cracks on the former part, while the latter part corresponds to the areas prone to ice avalanches.

(2) The glacier moving velocity was strongly correlated with the slope when ice avalanches were excluded. Generally, the glacier velocity increased with the increment of the slope, until the slope was large enough for an ice avalanche, where the glacier's moving velocity decreased rapidly. Some other reasons may also contribute to the velocity decrement: on the one hand, ice avalanches may reduce the signal-to-noise ratio of the POT result and thus distort the estimated velocity; on the other hand, the front channel of the ice cascade being narrow may also impede the glacier's movement.

(3) The glacier moving velocity had a positive correlation with the average daily maximum temperature, which passed the Monte Carlo testing under the significant level of $\alpha = 0.1$, especially in the area with very little possibility of forming an ice avalanche.

(4) The Luding earthquake did not increase the Hailuogou Glacier's moving velocity to a large extent. However, it did impact the front of the ice cascade. The susceptibility to large-scale ice avalanches was estimated as being low, and the buffering in the downstream glacier tongue further reduces the risk of ice avalanches. Nevertheless, the sediment in the gully became smaller in size and larger in quantity after the earthquake, the gully became narrower, and therefore the infiltration and runoff conditions have become more sensitive to floods, which all provide positive conditions to form a debris flow. Therefore, the investigation of the site and clearing the area of potential debris are essential to reduce the risk in the future.

(5) This study indicates that SAR offset tracking can be used not only for monitoring glacier movements under conventional conditions, but also for monitoring and evaluating the effects of strong earthquakes on glaciers. The methods used in this study may be the most efficient in the monitoring and assessment of seismic impact on glaciers, especially when high-resolution optical images are unavailable due to undesirable weather, or traffic blockages making site investigation unfeasible.

Author Contributions: Conceptualization, W.L. and J.C.; methodology, J.C. and H.L.; software, J.C. and Y.S.; validation, W.L. and H.L.; formal analysis, J.C. and C.Y.; investigation, H.L. and Y.S.; resources, Z.L. and X.D.; data curation, X.D.; writing—original draft preparation, J.C. and C.Y.; writing—review and editing, W.L.; visualization, Z.L.; supervision, W.L.; project administration, Q.X.; funding acquisition, W.L. All authors have read and agreed to the published version of the manuscript.

Funding: This research was funded by the National Key Research and Development Program of China, (Grant No. 2021YFC3000401) and the Key Research and Development Program of Sichuan Province (Grant No. 2023YFS0435). And the APC was funded by the National Key Research and Development Program of China, (Grant No. 2021YFC3000401).

Data Availability Statement: The datasets generated during and/or analyzed during the current study are available from the corresponding author on reasonable request.

Conflicts of Interest: The authors declare no conflict of interest.

References

1. China Earthquake Network Center. Available online: <https://www.cenc.ac.cn/> (accessed on 6 September 2022). (In Chinese)
2. Sichuan Earthquake Administration. Available online: http://www.scdzj.gov.cn/xwzx/fzjzyw/202210/t20221022_53715.html (accessed on 22 October 2022). (In Chinese)

3. Fan, X.; Wang, X.; Dai, L.; Fang, C.; Deng, Y.; Zou, C.; Tang, M.; Wei, Z.; Dou, X.; Zhang, J.; et al. Characteristics and spatial distribution pattern of Ms 6.8 Luding earthquake occurred on 5 September 2022. *J. Eng. Geol.* **2022**, *30*, 1504–1516. (In Chinese) [[CrossRef](#)]
4. Büyüksaraç, A.; Isik, E.; Harirchian, E. A case study for determination of seismic risk priorities in Van (Eastern Turkey). *Earthq. Struct.* **2021**, *20*, 445–455. [[CrossRef](#)]
5. Gupta, K.; Satyam, N. Co-seismic landslide hazard assessment of Uttarakhand state (India) based on the modified Newmark model. *J. Asian Earth Sci.* **2022**, *8*, 100120. [[CrossRef](#)]
6. Kumar, S.; Gupta, V.; Kumar, P.; Sundriyal, Y.P. Coseismic landslide hazard assessment for the future scenario earthquakes in the Kumaun Himalaya, India. *Bull. Eng. Geol. Environ.* **2021**, *80*, 5219–5235. [[CrossRef](#)]
7. Du, G.; Zhang, Y.; Zou, L.; Yang, Z.; Yuan, Y.; Ren, S. Co-seismic landslide hazard assessment of the 2017 Ms 6.9 Milin earthquake, Tibet, China, combining the logistic regression–information value and Newmark displacement models. *Bull. Eng. Geol. Environ.* **2022**, *81*, 1–7. [[CrossRef](#)]
8. Li, Z.; Sun, J.; Gao, M.; Fu, G.; An, Z.; Zhao, Y.; Fang, L.; Guo, X. Evaluation of horizontal ground motion waveforms at Sedongpu Glacier during the 2017 M6. 9 Mainling earthquake based on the equivalent Green's function. *Eng. Geol.* **2022**, *306*, 106743. [[CrossRef](#)]
9. Wu, Y.; Li, L.; Chen, C.; Liang, H.; Guo, N.; Li, Y. GNSS deformation characteristics of North China in the past two decades. *Geod. Geodyn.* **2021**, *12*, 392–398. [[CrossRef](#)]
10. Lazos, I.; Sboras, S.; Chousianitis, K.; Bitharis, S.; Mouzakiotis, E.; Karastathis, V.; Pikridas, C.; Fotiou, A.; Galanakis, D. Crustal deformation analysis of Thessaly (central Greece) before the March 2021 earthquake sequence near Ellassona-Tyrnavos (northern Thessaly). *Acta Geodyn. Geomater.* **2021**, *18*, 379–385. [[CrossRef](#)]
11. Shen, Z. Satellite geodesy applied to geodynamic and seismological studies in East Asia: A review. *Chin. J. Geophys.* **2021**, *64*, 3514–3520, (In Chinese with English Abstract)
12. Li, G.; Li, Y.; Lin, H.; Ye, Q.; Jiang, L. Two periods of geodetic glacier mass balance at Eastern Nyainqentanglha derived from multi-platform bistatic SAR interferometry. *Int. J. Appl. Earth Obs. Geoinf.* **2021**, *104*, 102541. [[CrossRef](#)]
13. Liu, G.; Li, J.; Xu, Z.; Wu, J.; Chen, Q.; Zhang, H.; Zhang, R.; Jia, H.; Luo, X. Surface deformation associated with the 2008 Ms8. 0 Wenchuan earthquake from ALOS L-band SAR interferometry. *Int. J. Appl. Earth Obs. Geoinf.* **2010**, *12*, 496–505. [[CrossRef](#)]
14. Xiao, R.; Jiang, M.; Li, Z.; He, X. New insights into the 2020 Sardoba dam failure in Uzbekistan from Earth observation. *Int. J. Appl. Earth Obs. Geoinf.* **2022**, *107*, 102705. [[CrossRef](#)]
15. Cai, J.; Zhang, L.; Dong, J.; Wang, C.; Liao, M. Polarimetric SAR pixel offset tracking for large-gradient landslide displacement mapping. *Int. J. Appl. Earth Obs. Geoinf.* **2022**, *6*, 248–249. [[CrossRef](#)]
16. Jiang, M.; Li, Z.W.; Ding, X.L.; Zhu, J.J.; Feng, G.C. Modeling minimum and maximum detectable deformation gradients of interferometric SAR measurements. *Int. J. Appl. Earth Obs. Geoinf.* **2011**, *13*, 766–777. [[CrossRef](#)]
17. Jiang, M.; Guarnieri, A.M. Distributed scatterer interferometry with the refinement of spatiotemporal coherence. *IEEE Trans. Geosci. Remote Sens.* **2022**, *58*, 3977–3987. [[CrossRef](#)]
18. Radicioni, F.; Stoppini, A.; Brigante, R.; Fornaro, G.; Bovenga, F.; Nitti, D.O. Long-Term GNSS and SAR Data Comparison for the Deformation Monitoring of the Assisi Landslide. In Proceedings of the FIG Working Week, Rome, Italy, 6–10 May 2012.
19. Ramzan, U.; Fan, H.; Aeman, H.; Ali, M.; Al-qaness, M.A.A. Combined analysis of PS-InSAR and hypsometry integral (HI) for comparing seismic vulnerability and assessment of various regions of Pakistan. *Sci. Rep.* **2022**, *12*, 1–24. [[CrossRef](#)]
20. Michel, R.; Rignot, E. Flow of Glacier Moreno, Argentina, from repeat-pass Shuttle Imaging Radar images: Comparison of the phase correlation method with radar interferometry. *J. Glaciol.* **1999**, *45*, 93–100. [[CrossRef](#)]
21. Yuan, W.; Ran, G.; Zhang, H. Genetic analysis of Hailuogou hot spring. *Min. Mag.* **2015**, *4*, 83–87, (In Chinese with English Abstract)
22. Li, Q.; Huang, G.; Nie, Z.; Chang, H. Research on slope defects of roadbeds in Hailuogou scenic area. *Road Transp. Technol.* **2012**, *10*, 59–61+64. (In Chinese)
23. Allen, C.R.; Zhuoli, L.; Hong, Q.; Xueze, W.; Huawei, Z.; Weishi, H. Field study of a highly active fault zone: The Xianshuihe fault of southwestern China. *Geol. Soc. Am. Bull.* **1991**, *103*, 1178–1199. [[CrossRef](#)]
24. Xu, J.; Li, J.; Yuan, Z.; Yao, W.; Zhang, J.; Ji, L.; Shao, Z.; Han, L.; Wang, Z. Airborne LiDAR-Based Mapping of Surface Ruptures and Coseismic Slip of the 1955 Zheduotang Earthquake on the Xianshuihe Fault, East Tibet. *Bull. Seismol. Soc. Am.* **2022**, *112*, 3102–3120. [[CrossRef](#)]
25. Zhou, R.; He, Y.; Huang, Z.; Li, X.; Yang, T. The Slip Rate and Strong Earthquake Recurrence Interval on the Qianning-Kangding Segment of the Xianshuihe Fault Zone. *Acta Seismol. Sin.* **2001**, *23*, 250–261. (In Chinese) [[CrossRef](#)]
26. Cheng, J.; Xu, X. Features of earthquake clustering form calculation of Coulmb stress around the Bayan Har Block, Tibetan Plateau. *Seismol. Geol.* **2018**, *40*, 133–154. (In Chinese) [[CrossRef](#)]
27. Liu, G.; Zhang, B.; Zhang, R.; Cai, J.; Fu, Y.; Liu, Q.; Yu, B.; Li, Z. Monitoring Dynamics of Hailuogou Glacier and the Secondary Monitoring Dynamics of Hailuogou Glacier and the Secondary Landslide Disasters Based on Combination of Satellite SAR and Ground-Based SAR. *Geomat. Inf. Sci. of Wuhan Univ.* **2019**, *44*, 980–995. (In Chinese) [[CrossRef](#)]
28. Zhang, Y.; Fujita, K.; Liu, S.; Liu, Q.; Wang, X. Multi-decadal ice-velocity and elevation changes of a monsoonal maritime glacier: Hailuogou glacier, China. *J. Glaciol.* **2010**, *56*, 65–74. [[CrossRef](#)]

29. He, Y.; Li, Z.; Yang, X.; Jia, W.; He, X.; Song, B.; Zhang, N.; Liu, Q. Changes of the Hailuogou Glacier, Mt. Gongga, China, against the Background of Global Warming in the Last Several Decades. *J. China Univ. Geosci.* **2008**, *19*, 271–281. [[CrossRef](#)]
30. Li, Z.; He, Y.; Yang, X.; Theakstone, W.H.; Jia, W.; Pu, T.; Liu, Q.; He, X.; Song, B.; Zhang, N.; et al. Changes of the Hailuogou glacier, Mt. Gongga, China, against the background of climate change during the Holocene. *Quat. Int.* **2008**, *218*, 166–175. [[CrossRef](#)]
31. Planet. Available online: <https://www.planet.com/explorer/> (accessed on 12 September 2022).
32. European Space Agency. Available online: <https://www.esa.int/> (accessed on 10 September 2022).
33. Torres, R.; Snoeij, P.; Geudtner, D.; Bibby, D.; Davidson, M.; Attema, E.; Potin, P.; Rommen, B.; Floury, N.; Brown, M.; et al. GMES Sentinel-1 mission. *Remote Sens. Environ.* **2012**, *120*, 9–24. [[CrossRef](#)]
34. Tianqi. Available online: www.lishi.tianqi.com (accessed on 2 October 2022).
35. Michel, R.; Avouac, J.; Taboury, J. Measuring ground displacements from SAR amplitude images: Application to the Landers earthquake. *Geophys. Res. Lett.* **1999**, *26*, 875–878. [[CrossRef](#)]
36. Wegmüller, U.; Werner, C.; Strozzi, T.; Wiesmann, A.; Frey, O.; Santoro, M. Sentinel-1 IWS Mode Support in the GAMMA Software. In Proceedings of the IEEE 5th Asia-Pacific Conference on Synthetic Aperture Radar (APSAR), Singapore, 1–4 September 2015.
37. Strozzi, T.; Luckman, A.; Murray, T.; Wegmüller, U.; Werner, C.L. Glacier motion estimation using SAR offset-tracking procedures. *IEEE Trans. Geosci. Remote Sens.* **2002**, *40*, 2384–2391. [[CrossRef](#)]
38. Alean, J. Ice avalanche activity and mass balance of a high-altitude hanging glacier in the Swiss Alps. *Ann. Glaciol.* **1985**, *6*, 248–249. [[CrossRef](#)]
39. Yu, B.; Yang, L.; Chang, M.; van Asch, T.W.C. A new prediction model on debris flows caused by runoff mechanism. *Environ. Earth Sci.* **2021**, *80*, 1–11. [[CrossRef](#)]
40. Zhang, G.; Cui, P.; Jin, W.; Zhang, Z.; Wang, H.; Bazai, N.A.; Li, Y.; Liu, D.; Pasuto, A. Changes in hydrological behaviours triggered by earthquake disturbance in a mountainous watershed. *Sci. Total Environ.* **2021**, *760*, 143349. [[CrossRef](#)] [[PubMed](#)]
41. Shi, Y.; Yang, Z.; Xie, Z.; Du, R. The glacial debris flow in Guxiang, Tibet. *Chin. Sci. Bull.* **1964**, *6*, 542–544. (In Chinese)

Disclaimer/Publisher’s Note: The statements, opinions and data contained in all publications are solely those of the individual author(s) and contributor(s) and not of MDPI and/or the editor(s). MDPI and/or the editor(s) disclaim responsibility for any injury to people or property resulting from any ideas, methods, instructions or products referred to in the content.